

**Enhancement of phonon skew scattering in epitaxial Pt/Co/Pt trilayers by crystal engineering**

Jie Qi <sup>1</sup>, Yunchi Zhao,<sup>2,\*</sup> Haochang Lyu <sup>1,2</sup>, Guang Yang <sup>3</sup>, He Huang,<sup>1</sup> Jingyan Zhang,<sup>1</sup> Jianxin Shen,<sup>1</sup> Weidu Qin,<sup>4</sup> Chaoqun Hu,<sup>4</sup> Yang Gao,<sup>4</sup> Yaqin Guo,<sup>4</sup> Bokai Shao,<sup>1</sup> Yi Zhang,<sup>1</sup> Zhaozhao Zhu,<sup>2</sup> Hongxiang Wei,<sup>2</sup> Baogen Shen,<sup>2</sup> and Shouguo Wang <sup>1,†</sup>

<sup>1</sup>Beijing Advanced Innovation Center for Materials Genome Engineering, School of Materials Science and Engineering, University of Science and Technology Beijing, Beijing 100083, China

<sup>2</sup>Beijing National Laboratory for Condensed Matter Physics, Institute of Physics, Chinese Academy of Sciences, Beijing 100190, China

<sup>3</sup>Department of Materials Science & Metallurgy, University of Cambridge, 27 Charles Babbage Road, Cambridge CB3 0FS, United Kingdom

<sup>4</sup>Institute of Advanced Materials, Beijing Normal University, Beijing 100875, China



(Received 29 August 2021; revised 22 November 2021; accepted 25 November 2021; published 13 December 2021)

Three types of (111)-oriented Pt/Co/Pt trilayers with single-crystalline structures on MgO substrates were fabricated to investigate the mechanisms of the anomalous Hall effect. By introducing 2-monolayer (ML) Cr insertion between a MgO (001) substrate and a Pt underlayer in Pt/Co/Pt epitaxial structures, the Hall resistivity is significantly enhanced compared with that of single-crystalline Pt/Co/Pt deposited on a MgO (111) surface. Furthermore, the detailed crystalline structures were characterized by *in situ* reflection high-energy electron diffraction, low-energy electron microscopy, and low-energy electron diffraction. It suggests that a twinning structure of the 7-ML ferromagnetic Co layer, which is composed of two twinned traces differing by 90°, can be achieved by crystal engineering with Cr insertion. By fitting with proper scaling of anomalous Hall effect, the dominant contribution to the Hall resistivity can be confirmed as skew scattering, and the remarkable enhancement of  $\rho_{xy}$  is attributed to the high phonon skew scattering parameter originating from the specific twinning structure.

DOI: [10.1103/PhysRevB.104.214417](https://doi.org/10.1103/PhysRevB.104.214417)

**I. INTRODUCTION**

It is widely recognized that the spintronic device with perpendicular magnetic anisotropy (PMA) has been a prominent topic in condensed matter physics for decades [1–8]. The anomalous Hall effect (AHE) has attracted great interest due to its abundant physical mechanism [9–12] and broad applications for sensors and memories [13–16]. It is worth pointing out that most of the theoretical studies of AHE have been performed based on single-layer films with in-plane magnetic anisotropy [8,14,17–21], while magnetic multilayers with PMA are beneficial for practical application [7,13,22–24]. Therefore, it is necessary further clarify the detailed mechanism of AHE in multilayers with PMA to promote the performance of related spintronic devices. Three mechanisms giving rise to AHE with different relationships between the transverse resistivity ( $\rho_{xy}$ ) and the longitudinal resistivity ( $\rho_{xx}$ ) have been identified: (1) The intrinsic anomalous velocity ( $\rho_{xy} \propto \rho_{xx}^2$ ) results from spin-orbit interaction of spin-polarized conduction electrons, which is perpendicular to the electric field [9]. Chang and Niu later formulated the model linking the intrinsic anomalous velocity to the Berry curvature of the electronic band structure in momentum space [25]. (2) The extrinsic contribution corresponding to skew scattering

( $\rho_{xy} \propto \rho_{xx}$ ) is attributed to the asymmetric scattering rate from impurities caused by spin-orbit coupling (SOC) which tends to have a dominant role in nearly perfect crystals [10]. (3) Furthermore the main source of the AHE current argued by Berger is the extrinsic contribution from side jump scattering ( $\rho_{xy} \propto \rho_{xx}^2$ ) which is viewed as a sidestep type of scattering arising from a sidewise shift of the center of the electron wave packet caused by the extrinsic SOC [12]. Among the three mechanisms, skew scattering will become dominant for AHE in the limit of small disorder because of the linear scaling of the skew scattering driven transverse resistivity with the longitudinal resistivity [26].

Recent progress on the AHE mechanism has provided a more complete framework for understanding this subtle phenomenon and has, in many instances, replaced controversy by clarity [17,27–29]. According to the Matthiessen rule, two components originating from residual skew scattering and phonon skew scattering will contribute to the skew scattering resistivity. A theoretical study by Tian *et al.* also pointed out that phonons should have a smaller role in skew scattering [17,30]. To clarify the physical intension of the phonon skew scattering in experiments, a specific system with considerable phonon scattering contribution of AHE is required to be established. Moreover, it is reasonable to investigate the AHE in a single-crystalline system with a low-disordered and tunable structure. Moreover, the Pt/Co bilayered system is an appropriate candidate due to strong spin-orbit coupling and perpendicular magnetic anisotropy [31–35].

\*yczhao@iphy.ac.cn

†sgwang@ustb.edu.cn

In this work, the mechanisms of AHE with a focus on skew scattering were investigated in epitaxial Pt/Co multilayers with specific crystalline structures and remarkable PMA. With 2 monolayers (ML) insertion of Cr, a specific structure with two twinned traces differing by  $90^\circ$  can be formed by crystal engineering which results in an enhanced contribution of skew scattering to anomalous Hall resistivity. By extracting the contributions of the physical mechanism with the acknowledged scaling of AHE [17], the skew scattering contribution is dominant in the anomalous Hall resistance and the increase of the anomalous Hall resistance can be attributed to the phonon skew scattering. This work is of vital importance to understand the physical mechanism of phonon skew scattering in AHE, and provides a promising approach to promote the performance of the spintronic devices by tailoring crystal structures.

## II. EXPERIMENTAL METHODS

**Thin-film fabrication.** The epitaxial films were deposited onto polished MgO (111) and MgO (001) single-crystal substrates using a molecular beam epitaxy (MBE) system with a base pressure superior to  $7.0 \times 10^{-11}$  mbar. The MgO substrates were cleaned by acetone and isopropanol in an ultrasound bath and annealed at  $750^\circ\text{C}$  for 2 h in the MBE chamber prior to the deposition. One of the MgO (001) substrates had 2-ML Cr inserted to regulate the interface lattice stress. A 36-ML Pt layer was directly deposited on the surface of the MgO (111) and MgO (001) substrates at  $100^\circ\text{C}$  and was annealed for half an hour at  $600^\circ\text{C}$  to release the lattice stress and to flatten the surface. Afterwards, a 7-ML Co layer and an 11-ML Pt layer were epitaxially deposited at  $100^\circ\text{C}$  successively. The top Pt layer was chosen to avoid the degradation of Co, and to ensure a high quality of epitaxial crystalline structure. The deposition rates for Pt and Co layers were controlled to be 0.048 and 0.028  $\text{\AA}/\text{s}$ , respectively. The films were patterned into Hall bar devices using standard photolithography and etching processes. The width of the Hall bar was 30  $\mu\text{m}$ .

**Measurements.** The formation of epitaxial structure and the high-quality surface was identified by *in situ* reflection high-energy electron diffraction (RHEED) and *ex situ* x-ray diffraction (XRD) with Cu  $K\alpha$  radiation ( $\lambda = 1.542 \text{\AA}$ ). The electric transport measurements at different temperatures were carried out using a physical property measurement system (PPMS DynaCool-14T). The low-energy electron diffraction (LEED) data were acquired on a low-energy electron microscopy (LEEM) system with a base pressure greater than  $3 \times 10^{-10}$  mbar which is connected to the MBE chamber. Therefore, the sample can be immediately transferred to the LEEM analysis chamber after deposition. A 5  $\mu\text{m}$  sized microdiffraction aperture was used to control the size of the incoming electron beam through the prism to the sample, which leads to the spot size of the microscope being limited to 185 nm on the sample, less than the size of the crystal domain.

## III. RESULTS AND DISCUSSIONS

For the epitaxial growth of Pt on MgO substrates, there is a parallel alignment between the epitaxial orientation of the Pt

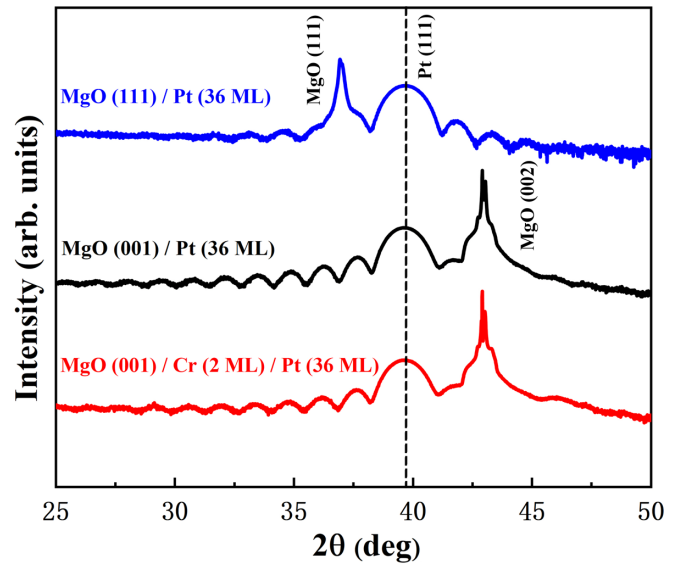


FIG. 1. XRD  $\theta$ - $2\theta$  scan for 36-ML Pt films deposited on MgO (111) (blue line), MgO (001) (black line), and MgO (001)/Cr (2 ML) (red line), respectively. All peaks are calibrated based on a standard powder diffraction file (PDF) card of MgO for XRD with Cu  $K\alpha$  radiation. The black dashed line marks the  $2\theta$  of Pt (111) peak from standard spectra ( $39.76^\circ$ ).

layer and MgO (111) substrates. However, a similar (111)-oriented structure still can be formed of Pt directly grown onto a MgO (001) surface at low deposition temperature due to the interfacial energy minimum [36,37]. In addition, the formation of (111) orientation of Pt can still be achieved when 2 monolayers (ML) of Cr was introduced between the Pt underlayer and the MgO (001) substrate. This can be confirmed by the x-ray diffraction (XRD) patterns as shown in Fig. 1. The strong Pt (111) diffraction peaks and multiple interference peaks can be clearly observed in XRD patterns of a 36-ML Pt layer epitaxially deposited on MgO (111), MgO (001), and MgO (001)/Cr (2 ML) substrates, indicating high-quality epitaxy of single-crystalline structure. The peak of Pt is calibrated to be  $39.61^\circ$ ,  $39.71^\circ$ , and  $39.59^\circ$  on MgO (111), MgO (001), and MgO (001)/Cr (2 ML), respectively. All peaks are in good agreement with the standard spectra of which the peak of Pt (111) is located at  $39.76^\circ$ , suggesting extremely small lattice distortion resulting from the lattice mismatch between the Pt layer and substrates. In addition, it is necessary to point out that the structural regulating effect by ultrathin Cr insertion between the MgO (001) substrate and the Pt layer is extremely sensitive to the thickness of the Cr insertion. For example, a specific polycrystalline state with the coexistence of a (111) plane and a (001) plane for the Pt layer can be induced when the thickness of the Cr insertion is increased to 3 ML. More detailed information can be found in the Supplemental Material (Figs. S1 and S2) [38] (also see [39]).

Due to the proximate lattice constant of Co and Pt, the epitaxial orientation of Co can be determined by the Pt underlayer. Therefore, a 7-ML Co layer was epitaxially deposited on (111)-oriented Pt surfaces with slightly different distortions mentioned above to investigate the AHE affected by

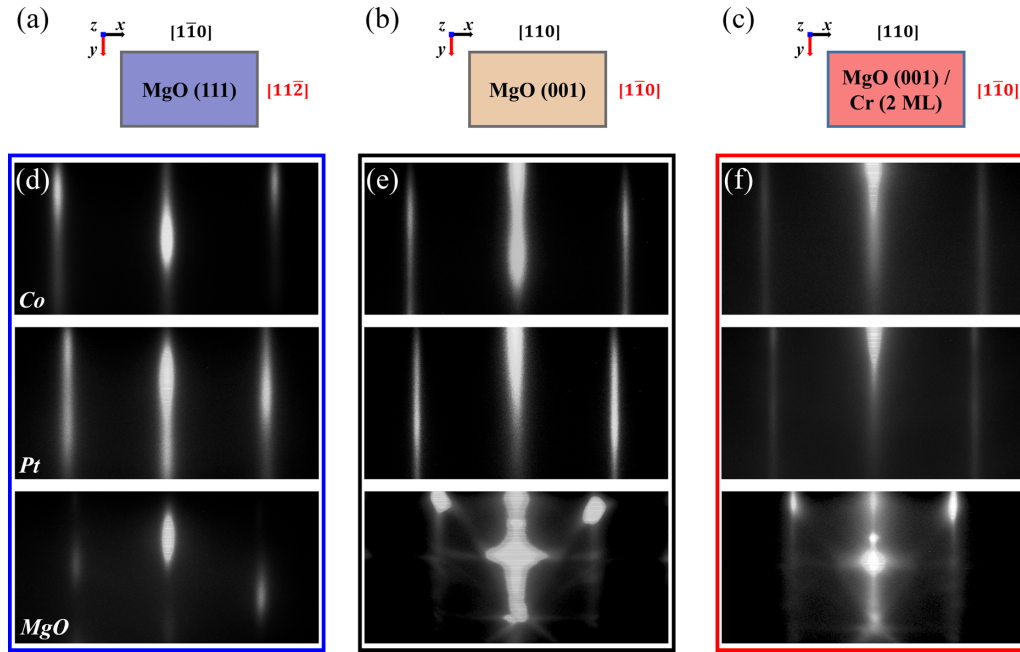


FIG. 2. Schematic diagram for MgO substrates (a) S1, (b) S2, and (c) S3. RHEED patterns for (d) 7-ML Co, 36-ML Pt, and MgO (111) substrate for S1; (e) 7-ML Co, 36-ML Pt, and MgO (001) substrate for S2; (f) 7-ML Co, 36-ML Pt, and MgO (001)/Cr substrate for S3 with  $e$  beam along MgO  $[1\bar{1}0]$  orientation for MgO (111) and MgO  $[110]$  orientation for MgO (001) substrates, respectively.

the crystalline structure. Three samples were grown with the structure of Pt (36 ML)/Co (7 ML)/Pt (11 ML) on MgO (111) (sample called S1), MgO (001) (S2), and MgO (001)/Cr (2 ML) (S3) substrates, respectively. The deposition processions were monitored by *in situ* reflection high-energy electron diffraction (RHEED) with the incident electron beam parallel to the  $x$  axis defined in Figs. 2(a)–2(c). The sharp and continuous diffraction streaks shown in Fig. 2 demonstrate a high-quality epitaxial growth corresponding to S1 [Fig. 2(d)], S2 [Fig. 2(e)], and S3 [Fig. 2(f)], respectively. The lattice constants of the Pt ( $a_{\text{Pt}} = 3.92 \text{ \AA}$ ) and Co ( $a_{\text{Co}} = 3.55 \text{ \AA}$ ) layers with face-centered cubic (fcc) crystalline structure were calculated in accordance with the distance between the specular streak and the first-order diffraction streak of the RHEED patterns by the reciprocal relationship between real and reciprocal spaces. Therefore, the constants were calculated to be  $a_{\text{Pt1}} = 3.90 \text{ \AA}$  and  $a_{\text{Co1}} = 3.58 \text{ \AA}$  on a MgO (111) substrate,  $a_{\text{Pt2}} = 3.81 \text{ \AA}$  and  $a_{\text{Co2}} = 3.49 \text{ \AA}$  on a MgO (001) substrate, and  $a_{\text{Pt3}} = 3.83 \text{ \AA}$  and  $a_{\text{Co3}} = 3.57 \text{ \AA}$  on a MgO (001)/Cr (2 ML) substrate, respectively. The lattice distortion between the 36-ML epitaxial Pt layer and the standard bulk Pt with fcc crystalline structure can be defined as  $\Delta a = (a_{\text{Pt}i} - a_{\text{Pt}})/a_{\text{Pt}}$ , where  $a_{\text{Pt}i}$  ( $i = 1, 2, \text{ or } 3$ ) and  $a_{\text{Pt}}$  correspond to the crystal constant of the 36-ML Pt layer and bulk Pt with fcc crystalline structure ( $3.92 \text{ \AA}$ ). The lattice distortions of the Pt layer were estimated to be  $-0.51\%$  (S1),  $-2.81\%$  (S2), and  $-2.30\%$  (S3), respectively, indicating a small lattice mismatch between the Pt layer and substrates, in good agreement with XRD results. Similarly, the estimated distortion of the Co layers was  $0.85\%$  (S1),  $-1.69\%$  (S2), and  $0.56\%$  (S3), respectively. It can be noticed that with 2-ML Cr insertion, the distortion due to the relaxation of the interfacial lattice stress of the Pt layer

and the Co layer in sample S3 can be suppressed between the Pt layer and the substrates compared to that of S2.

Based on the (111)-oriented growth of Pt/Co, the AHE in the three epitaxial samples with good PMA were investigated by transport measurements. Figure 3(a) illustrates the geometry of Hall measurement, where the AHE loops are obtained by measuring the Hall resistance ( $R_{xy}$ ) by sweeping the magnetic fields parallel to the  $z$  axis with current injection along the  $x$  axis. The evidence of PMA can be directly seen from a square hysteresis loop of AHE measurement. Figures 3(b)–3(d) present the hysteresis loops for samples S1–S3 at various temperatures ranging from 2 to 300 K. The sharp and square loops indicate that the PMA can be well maintained at the whole range of temperature for three samples. It should be emphasized that an obvious change of  $R_{xy}$  values at 300 K [room temperature (RT)] can be seen, which is 75.6, 68.6, and  $106.3 \text{ m}\Omega$  for S1–S3, respectively. The  $R_{xy}$  of sample S3 with 2-ML Cr insertion at RT is 40.6% larger than that of the S1 and 55.0% compared to S2. Furthermore, the value of  $R_{xy}$  decreases with decreasing temperature, which is 1.27, 6.49, and  $21.28 \text{ m}\Omega$  at 2 K for S1–S3, respectively. The enhanced ratio for S3 is 1576% and 228% at 2 K compared to S1 and S2, respectively.

Moreover, the detailed mechanism of AHE in multilayers can be further clarified by analyzing the transport results. Figure 4(a) shows the anomalous Hall resistivity ( $\rho_{xy}$ ) as a function of temperature (2–300 K). The value of  $\rho_{xy}$  for three samples shows a monotonic decrease with decreasing temperature. The  $\rho_{xy}$  of S3 is much larger than that of S1 and S2 in the whole range of temperature. In particular, Fig. 4(b) shows the AHE loops of three samples at 2 K, indicating an extreme difference of  $R_{xy}$  at low temperatures.

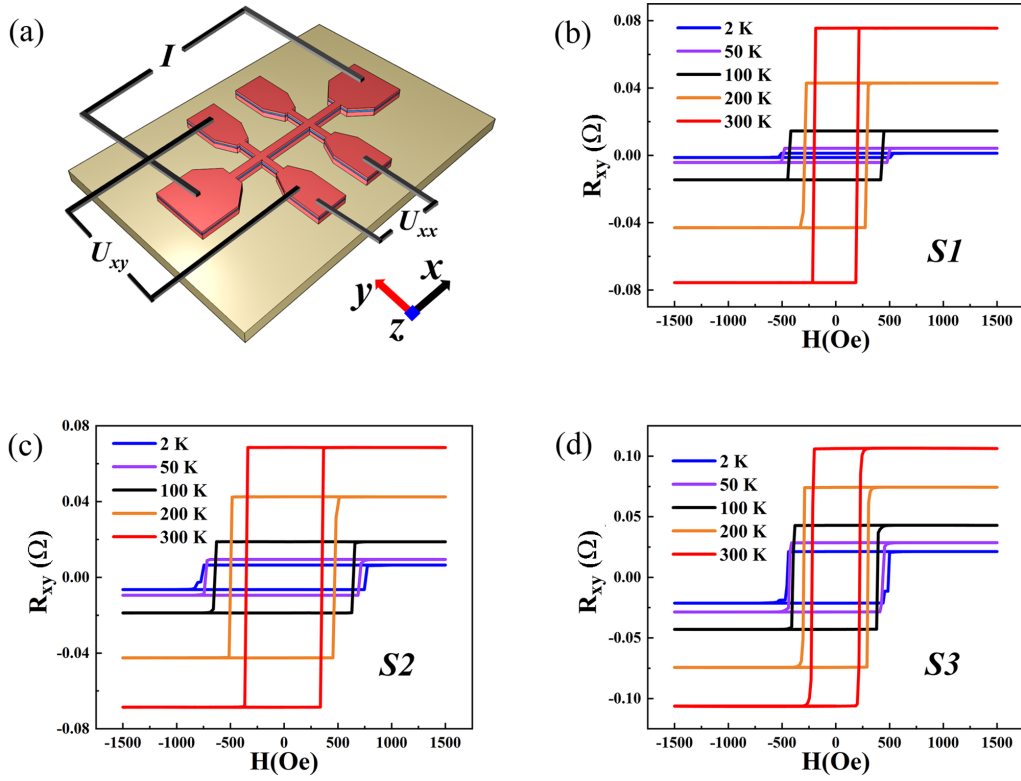


FIG. 3. (a) Schematic setup for AHE measurements. (b)–(d) AHE loops at different temperatures ranging from 2 to 300 K for (b) S1, (c) S2, and (d) S3, respectively.

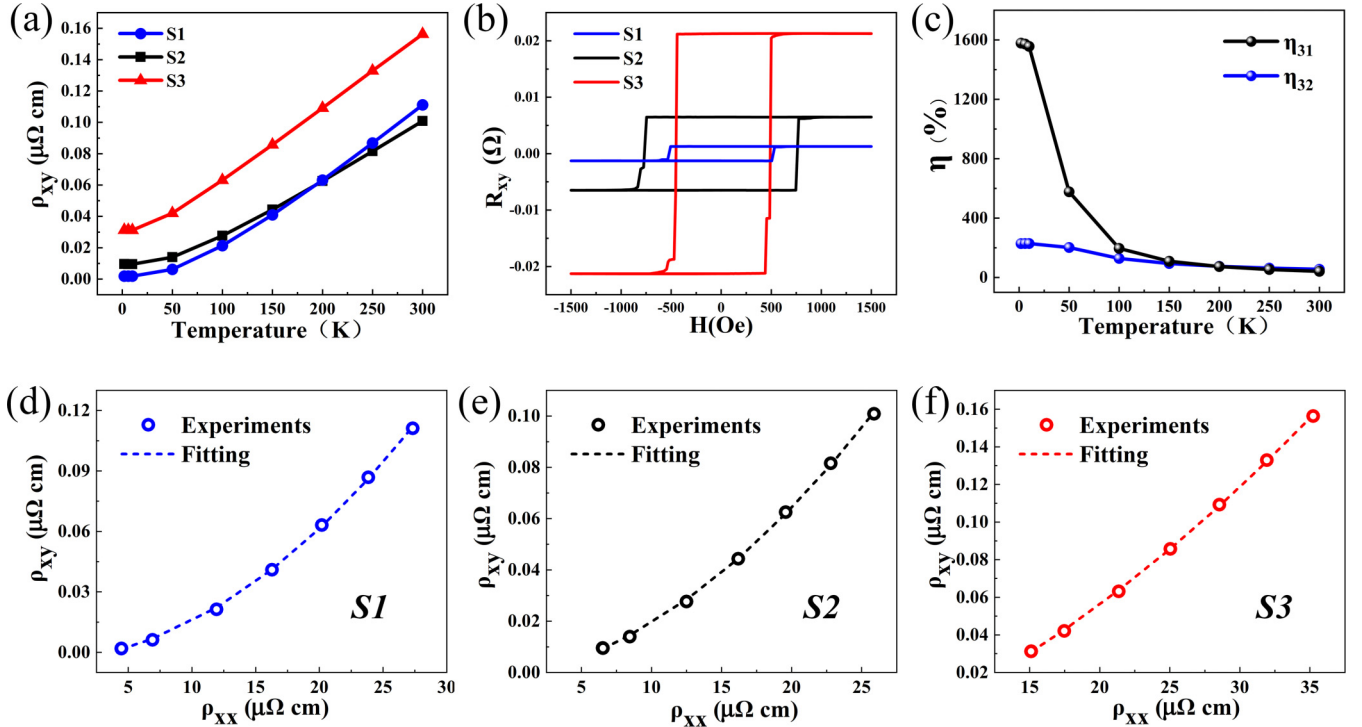


FIG. 4. (a)  $\rho_{xy}$  as functions of temperature for three samples ranging from 2 to 300 K. (b) AHE loops of S1, S2, and S3 at 2 K. (c) Temperature dependence of  $\eta_{31}$  and  $\eta_{32}$  from 2 to 300 K. (d)–(f)  $\rho_{xy}$  vs  $\rho_{xx}$  curves for (d) S1, (e) S2, and (f) S3. Dashed line in (d)–(f) shows fitting results with  $\rho_{\text{AH}} = a' \rho_{xx0} + a'' \rho_{xx}(T) + b \rho_{xx}^2$ .

TABLE I. The extracted residual skew scattering coefficient  $a'$ , phonon skew scattering coefficient  $a''$ , side jump scattering, and intrinsic coefficient  $b$  for three samples on different substrates.

Substrate	$a'$	$a''$	$b$ ( $\mu\Omega^{-1} \text{ cm}^{-1}$ )
MgO (111)	$-7.81 \times 10^{-4}$	$5.45 \times 10^{-4}$	$13.50 \times 10^{-5}$
MgO (001)	$-3.30 \times 10^{-4}$	$9.89 \times 10^{-4}$	$11.65 \times 10^{-5}$
MgO (001)/ Cr (2 ML)	$-16.49 \times 10^{-4}$	$26.0 \times 10^{-4}$	$7.27 \times 10^{-5}$

The change of anomalous Hall resistivity can be defined as

$$\eta_{ba} = (\rho_{xyb} - \rho_{xya})/\rho_{xya}(a, b = 1, 2, \text{ or } 3),$$

and the temperature dependence of the calculated  $\eta_{31}$  and  $\eta_{32}$  was shown in Fig. 4(c). Both  $\eta_{31}$  and  $\eta_{32}$  increase with decreasing temperature and  $\eta_{31}$  shows a tremendous slope compared to  $\eta_{32}$  at low temperatures. The  $\eta_{31}$  is enhanced from 40.6% at 300 K to 1576% at 2 K, indicating a significant impact of the structure in epitaxial Pt/Co bilayers on the contribution from various mechanisms. Furthermore, a crucial issue is the determination of the dominant mechanism responsible for the AHE enhancement in sample S3 with 2-ML Cr insertion between the Pt underlayer and MgO (001) substrate.

The measured  $\rho_{xy}$  and  $\rho_{xx}$  under various temperatures are then analyzed with the scaling law to separate the skew scattering, side jump scattering, and intrinsic contributions to the AHE in the multilayers. According to previous work [14,17,29,40], different scaling laws describing  $\rho_{xy}$  in terms of  $\rho_{xx}$  have been presented. For the widely used scaling  $\rho_{AH} = a\rho_{xx} + b\rho_{xx}^2$ , the contribution to  $\rho_{xy}$  from different mechanisms cannot be ideally separated by fitting the relationship between  $\rho_{xy}$  and  $\rho_{xx}$ , where  $a$  represents the contribution from skew scattering and  $b$  is the combined contribution from intrinsic Berry curvature and the extrinsic side jump mechanism. It reveals that the contribution of three mechanisms in the magnetic multilayers cannot be described perfectly with this conventional model, and more sophisticated terms need to be introduced to perform a clarification on AHE mechanisms in detail. By considering the separated contribution from residual and phonon skew scattering instead of one term in the conventional model, the modified fitting approach for the mechanisms contributing to the anomalous Hall resistivity can be described as  $\rho_{AH} = \rho_{SK} + b\rho_{xx}^2$ , where  $\rho_{SK} = a'\rho_{xx0} + a''\rho_{xx}(T)$  represents the combined contribution from residual and phonon skew scattering [17]. The first term  $a'$  reveals the contribution from residual skew scattering, the second term  $a''$  stands for the contribution from phonon skew scattering, and the last term  $b$  is the combined contribution from intrinsic Berry curvature and the extrinsic side jump mechanism. This formula is deployed for fitting to obtain  $a'$ ,  $a''$ , and  $b$  for three samples, which is shown in Figs. 4(d)–4(f), respectively. Here,  $\rho_{xx0}$  is approximated with  $\rho_{xx}$  at 2 K [17]. It clearly indicates that the relationship between  $\rho_{xx}$  and  $\rho_{xy}$  can be well fitted by applying the updated model. The fitted values of  $a'$ ,  $a''$ , and  $b$  are listed in Table I.

It is evident that the values of  $b$  for three samples are similar due to the limited thickness of the Co layer (7 ML). This can be attributed to the finite-size effect imposing a

limitation to the mean free path of electron scattering which suppresses the intrinsic contribution to anomalous Hall resistivity [22,41]. For all three structures,  $a'$  exhibits negative signs of  $a''$  and  $b$ , indicating that the residual skew scattering contributes to the anomalous Hall resistivity in the opposite way as the phonon skew scattering, side jump, and the intrinsic terms do. However,  $a'$  and  $a''$  are distinctly different. The value of  $a'$  was calculated as  $-7.81 \times 10^{-4}$ ,  $-3.30 \times 10^{-4}$ , and  $-16.49 \times 10^{-4}$  for sample S1–S3, respectively, indicating a larger residual skew scattering contribution to anomalous Hall resistivity of S3 compared to S1 and S2. It is necessary to point out that the contribution from residual skew scattering is independent of temperature, resulting in less effect on  $R_{xy}$  with varying temperature. On the other hand, the value of  $a''$  was  $5.45 \times 10^{-4}$ ,  $9.89 \times 10^{-4}$ , and  $26.0 \times 10^{-4}$  for S1–S3, respectively. The value of  $a''$  for sample S3 is much larger compared to S2 and S1, which demonstrates that the contribution of the phonon skew scattering is extremely enhanced in the Co layer of S3. At ultralow temperatures, the interactions, impurity scattering, and phonons contribute obviously to anomalous Hall resistance resulting in the maximum differentiation of  $\rho_{xy}$  values of the three structures at 2 K. By approximating  $\rho_{xx}$  at 2 K to be  $\rho_{xx0}$ , the  $\rho_{SK}$  originating from the extrinsic contributions of skew scattering were calculated to be  $-1.05 \times 10^{-3}$ ,  $4.30 \times 10^{-3}$ , and  $14.37 \times 10^{-3} \mu\Omega \text{ cm}$  for S1–S3, respectively. The opposite sign of  $\rho_{SK}$  at 2 K should correspond to the large differentiation of  $\rho_{xy}$ . According to the Matthiessen rule, the residual skew scattering contribution is independent of temperature in contrast with the phonon skew scattering contribution. The higher value of  $\rho_{xy}$  for S3 during the whole temperature range from 2 to 300 K demonstrates that the enhanced AHE in sample S3 originates from the phonon skew scattering contribution. In addition, it is necessary to note that the spin current generated in the ferromagnetic Co layer may penetrate into the adjacent Pt layer due to the high spin-orbit interaction in Pt causing the spin current proximity effect, which may result in an enhancement of the  $R_{xy}$  [42,43]. However, the contributions to  $R_{xy}$  from the spin current proximity effect should be negligible with weak spin current due to about 4% shunt in the Co layer and a relatively small spin Hall angle of the epitaxial Pt layer [44]. On the other hand, the magnetic proximity effect (MPE) which may introduce an additional contribution to  $R_{xy}$  was also considered [45]. The experimental results of vibrating sample magnetometer (VSM) measurement indicate that the  $M_S$  of S3 corresponding to the largest  $R_{xy}$  is even slightly smaller than that of S1 (more discussion can be found in Figs. S4 and S5 of the Supplemental Material [38]). Therefore, the spin current proximity effect and MPE in Pt/Co may not dominate the large enhancement of AHE in S3.

According to the previous study by Chen *et al.* [46],  $a''$  related to the phonon skew scattering process is mainly affected by long-range ordering. It is necessary to clarify that the detailed crystalline structures of three samples should be responsible for the extraordinary difference of  $a'$  and  $a''$ . Therefore, RHEED patterns in a wider view of (111)-oriented Pt underlayer and magnetic Co layer with 2-ML Cr insertion were further detected to clarify the structural contribution to skew scattering. Figure 5(a) shows the RHEED patterns of the 36-ML Pt underlayer and the 7-ML magnetic Co layer of S3

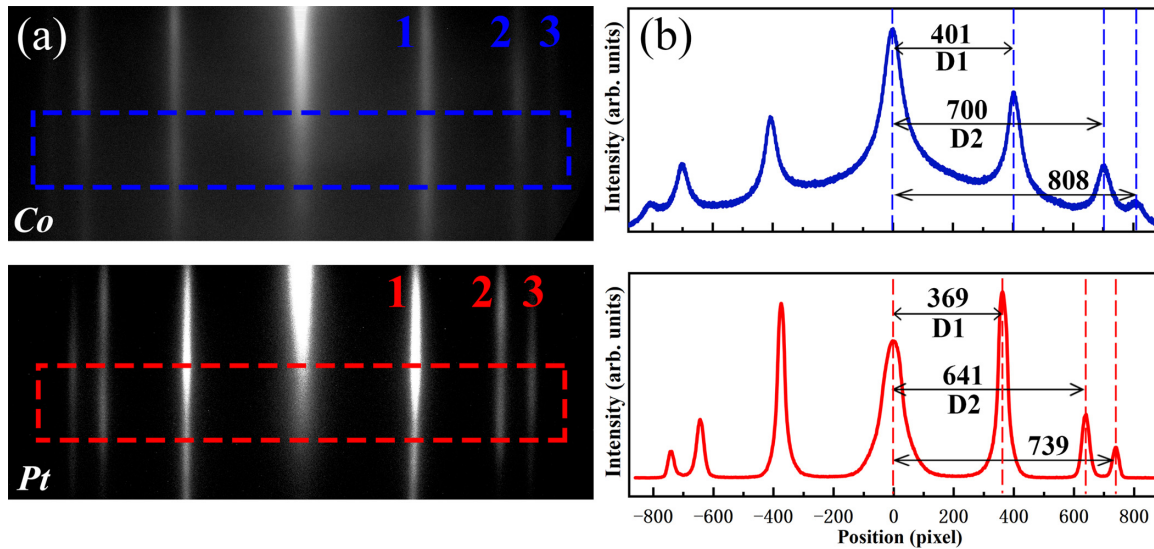


FIG. 5. (a) RHEED patterns of Pt underlayer and magnetic Co layer with 2-ML Cr insertion (S3) obtained with wide detection range. Three sets of diffraction streaks are marked as streak 1, streak 2, and streak 3. (b) The normalized intensity gray level of the selected areas on the (a) RHEED patterns of Pt underlayer (marked by the red rectangle) and Co layer (marked by the blue rectangle).

with a wider view suggesting an extra set of streaks (marked as streak 2) compared with the configuration of the Pt and Co layer on the MgO (111) surface (S1). Streak 2 appears between the first-order diffraction streaks (marked as streak 1) and the second-order diffraction streaks (marked as streak 3). Additionally, Fig. 5(b) gives the normalized intensity curves of the selected areas on the RHEED patterns [Fig. 5(a)] of the Pt underlayer (marked by the red rectangle) and the Co layer (marked by the blue rectangle). The proportional relationship in reciprocal space between streak 1 and streak 2 in the RHEED patterns of the Pt underlayer and the magnetic Co layer in S3 can be calculated as follows:

$$\frac{D_2}{D_1} = \frac{641}{369} = \frac{700}{401} \approx 1.732.$$

This value satisfies the reciprocal relationship with the ratio of interplanar spacing  $d_{110}$  and  $d_{112}$  of Pt and Co single crystals in real space. It is reasonable to conclude that the crystalline structure of the Co layer epitaxially deposited on the Pt surface is determined by that of the Pt underlayer. Therefore, a surface state of quasicrystalline structure with 12-fold symmetry or a twinning structure of the magnetic Co layer is speculated to be responsible for the extra set of streaks.

The crystalline symmetry of the three samples was further investigated by low-energy electron diffraction (LEED) and low-energy electron microscopy (LEEM) in order to confirm the detailed crystalline structure. Figure 6(a) shows the LEED pattern of the Pt underlayer deposited on the MgO (111) surface (S1) exhibiting sharp spots of the first-order diffraction with a sixfold intensity distribution, which originates from the close-packed layer structure of (111) orientation in the fcc structure. However, a 12-fold symmetry LEED pattern was observed from the (111)-oriented Pt surface directly deposited on the MgO (001) surface (S2) as shown in Fig. 6(b), different from the typical (111)-oriented LEED pattern of a Pt layer with sixfold symmetry. A similar 12-fold symmetric structure was confirmed in the system of Pt (5nm)/MgAl<sub>2</sub>O<sub>4</sub>

(001) [47]. The diffused diffraction spots are related to the relatively low degree of long-range ordering due to the lattice stress induced by mismatch between the (111)-oriented Pt layer and MgO (001) substrate. Furthermore, Fig. 6(c) shows the LEED pattern of the Pt underlayer on the MgO (001) surface with Cr insertion exhibiting sharp diffraction spots. This indicates an enhanced degree of crystallinity, consistent with the smaller lattice distortion of S3 compared to that of S2 as analyzed by the RHEED characterization. Therefore, S2 can be considered as the intermediate state of S1 and S3. It is worth noting that the anomalous Hall angle shows a clear dependence on the surface roughness according to the work by Zhang *et al.* [48]. However, the difference of roughness at the interface of the three samples can be negligible in this work due to the sharp diffraction patterns in RHEED and LEED. The topographic observation was performed in LEEM mode. Figure 6(d) shows the LEEM image of the 36-ML Pt layer on the MgO (111) surface. The well-spaced morphology with reasonably parallel stripes can be observed from the LEEM image, indicating the ultrasmooth surface. For the LEEM image of a Pt layer epitaxially grown on a MgO (001) surface with Cr insertion (S3) shown in Fig. 6(e), evenly arranged and mutually perpendicular atomic steps can be observed, which divides the Pt surface into a series of right-angled polygon areas in contrast with Fig. 6(d). To further investigate the microstructure of the Pt layer, a microdiffraction aperture is introduced to limit the size of the incident electron beam to the film to 185 nm, which is less than the size of the right-angled polygon areas. Figures 6(f) and 6(g) show the typical LEED patterns of a (111)-oriented Pt layer with a sixfold symmetry at the right-angled polygon areas marked by red and blue rectangles in the LEEM image shown in Fig. 6(e), respectively, of which the symmetries differ by 90°. It is reasonable to say that the 12-fold LEED pattern without the microdiffraction aperture [Fig. 6(d)] is a binary mixture of the above two types of intensity distributions resulting from a series of average twinning structures rather than a surface state

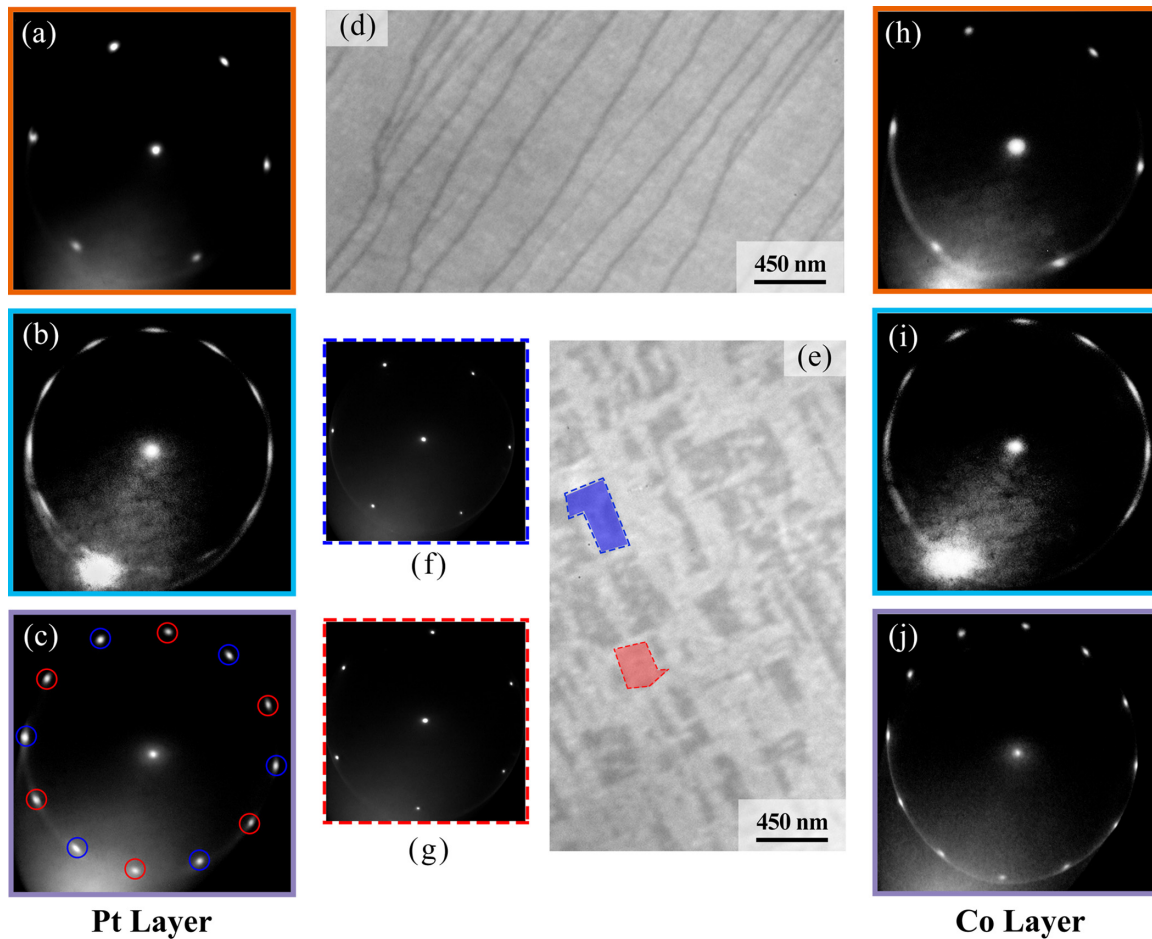


FIG. 6. (a)–(c) LEED patterns for 36-ML Pt of (a) S1, (b) S2, and (c) S3. LEEM images for 36-ML Pt of S1 (d) and S3 (e), respectively. LEED patterns of the selected areas of two twinned traces marked by (f) blue and (g) red right-angled polygon areas in Fig. 4(e). LEED patterns for 7-ML Co of (h) S1, (i) S2, and (j) S3. Red and blue circles in (c) represent two sets of diffraction spots originating from different crystal domains.

of quasicrystalline structure with similar 12-fold symmetry observed from an ultrathin BaTiO<sub>3</sub> layer on a (111)-oriented Pt surface [49]. The two twinned traces differ by 90° obtained from the reciprocal relationship between real and reciprocal spaces. It can be speculated that the observed morphology in Fig. 6(e) originates from surface atomic steps resulting from the grain boundary of the right-angled polygon areas corresponding to the different crystal domains. Thus, the different crystalline structures of (111)-oriented Pt are confirmed with typical single-crystalline structure for S1 and twinning structure for S3, respectively. Additionally, orientated growth of the Co layer is determined by the crystalline structure of the Pt underlayer with a parallel alignment of their epitaxial orientations. Furthermore, Figs. 6(h)–6(j) show the LEED patterns of the 7-ML Co layer epitaxially deposited on Pt of S1–S3, respectively. The crystal structure of the Co layer shows a sixfold symmetry for S1 [Fig. 6(h)] but 12-fold symmetry for S2 and S3 [Figs. 6(i) and 6(j)], which is consistent with the Pt underlayer as expected. Similarly, diffused diffraction spots are obtained in the LEED pattern of the Co layer for S2, but sharp diffraction spots are obtained in the LEED pattern for S3, indicating a higher degree of crystallinity for the magnetic Co layer with 2-ML Cr insertion.

According to the analysis of the RHEED patterns and LEED results above, the atoms of Pt and Co are arranged on a MgO (111) surface with sixfold symmetry as in the schematic drawing shown in Fig. 7(a). Additionally, the 2-ML Cr insertion introduced in S3 with a fourfold symmetric arrangement relaxes the interface lattice stress without changing the original (001) orientation of the MgO surface. Thus, the illustrations as shown in Fig. 7(b) suggest similar atomic arrangements of Pt/Co on MgO (001) and MgO (001)/Cr (2 ML) surfaces with fourfold symmetry. A (111)-oriented Pt underlayer and magnetic Co layer with sixfold symmetry can be formed for three samples with relatively small lattice distortion. Based on the arrangement of Pt atoms on substrates in S1–S3, the theoretical lattice mismatch ( $\epsilon$ ) between the Pt underlayer and substrates was calculated to be 7.34%, 7.32%, and 3.97% for S1–S3, respectively, and  $\epsilon$  is defined as  $\epsilon = (a_{\text{sub}} - a_{\text{flm}})/a_{\text{flm}}$ , where  $a_{\text{sub}}$  and  $a_{\text{flm}}$  correspond to the distance of the nearest-neighbor O (Cr) atoms of the substrate and bulk Pt. It is evident that the mismatch between the MgO substrate and the Pt underlayer in S3 is reduced because of the introduction of the 2-ML Cr insertion, which modulates the crystalline structure of the Co layer induced by the Pt underlayer. Therefore, a high-quality Co layer with high

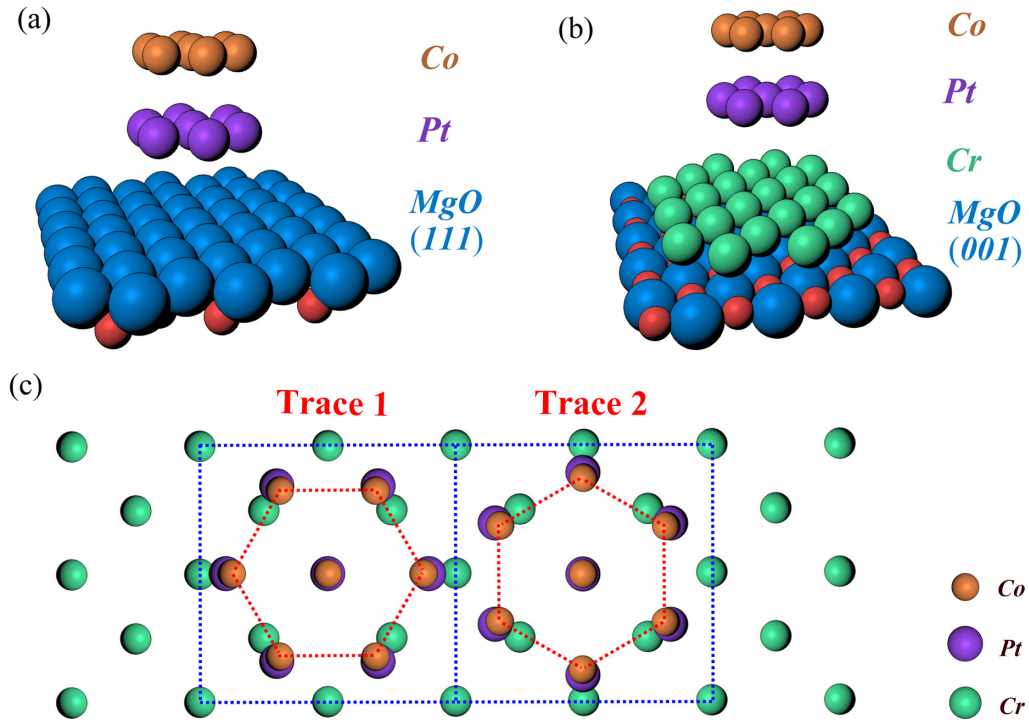


FIG. 7. Schematic drawing of Pt and Co with fcc crystallographic (111) plane on (a) MgO (111) and (b) MgO (001) and MgO (001)/Cr (2 ML). (c) Schematic drawing of the specific twinning structure of Pt (Co) with  $90^\circ$  twinned traces. Trace 1 and trace 2 are marked with blue rectangles and the symmetry of the crystal domain is marked with red regular hexagons.

crystallinity is formed in S3 consistent with the sharp spots in the LEED pattern and smaller lattice distortion calculated above. Furthermore, a crystalline model with a twinning structure can be established to explain the unique RHEED patterns of the Pt underlayer and the magnetic Co layer on a MgO (001) surface with 2-ML Cr insertion. Figure 7(c) shows the schematic drawing of the twinning structure and the  $e$ -beam incidence direction relationship meeting the above criteria. The twinned traces epitaxially grown MgO (001) surface with Cr insertion are marked by a red dashed rectangle, and the mutually perpendicular symmetry is illustrated with blue regular hexagons in Fig. 7(c). The  $e$  beam of RHEED is along the  $x$  axis, of which the spot size is far beyond the size of one twinned trace. Accordingly, two diffraction intensity contributions from the twinned traces in the RHEED patterns of the Pt and Co layer can be obtained with enough range of detection. As marked in Figs. 5(a) and 7(c), streak 2 originates from the first-order diffraction streak of the twinned trace 1, while streak 1 and streak 3 result from the first- and second-order diffraction streaks of the twinned trace 2, respectively.

Though the crystallinity of S3 is higher than that of S2 for its sharper LEED spots, the value of  $a''$  for sample S3 is enormously enhanced compared to S2 and S1, demonstrating that the twinning structure of Co can extremely enhance the contribution of the phonon skew scattering due to the existence of the grain boundaries between the specific  $90^\circ$  twinned traces. For phonons, the collisions originate from not only other phonons, but also from lattice defects, chemical impurities, grain boundaries, and rough edges, etc. [50]. A series of experimental and theoretical studies have proved that

both phonon scattering and electron-phonon interaction can be considerably affected by grain boundaries with a break of long-range ordering [50–52]. Therefore, it is reasonable to speculate that the slight enhancement of the phonon skew scattering in S2 compared with S1 is caused by the relatively low degree of long-range ordering, and for S3 with the 2-ML Cr insertion, the specific twinning structure with high degree of crystallinity and clear grain boundaries can be formed contributing dominantly to the large enhancement of AHE (40.6%). The physical mechanism of phonon scattering and electron-phonon interaction at the grain boundaries of the specific twinning structure should be further explored to have a deeper insight into the phonon skew scattering in AHE.

#### IV. CONCLUSION

In summary, the mechanism of anomalous Hall effect was investigated in (111)-oriented Pt/Co/Pt films with single-crystalline structures on MgO substrates. By introducing a 2-ML Cr insertion between MgO (001) substrate and Pt underlayer in Pt/Co/Pt epitaxial structure, a twinning structure of 7-ML ferromagnetic Co layer, which is composed of two twinned traces differing by  $90^\circ$ , can be achieved by crystal engineering. The  $\rho_{xy}$  corresponding to the sample with this specific structure is significantly enhanced. By fitting with proper scaling of AHE, the dominant contribution to the Hall resistivity can be confirmed as the skew scattering, and the remarkable enhancement of  $\rho_{xy}$  in S3 is attributed to the strengthened phonon skew scattering at the grain boundaries of the specific twinning structure. This work may shed light on the understanding of the mechanism of phonon skew scattering

in AHE, and provides a promising approach to promoting the on/off ratio of the AHE, hence the performance of the spintronic devices by tailoring crystal structures.

### ACKNOWLEDGMENTS

This work was supported by the National Key Research and Development Program of China (Grant No.

2019YFB2005800), the Natural Science Foundation of China (Grants No. 51625101, No. 52130103, No. 12174426, No. 11874082, and No. 51971026), the ISF-NSFC Joint Research Program (Grant No. 51961145305), the State Key Laboratory for Advanced Metals and Materials (Grant No. 2019Z-10), Beijing Natural Science Foundation Key Program (Grant No. Z190007), and the Fundamental Research Funds for the Central Universities Grant No. FRF-TP-16-001C2.

- 
- [1] L. Néel, Magnetic surface anisotropy and superlattice formation by orientation, *J. Phys. Radium* **15**, 225 (1954).
- [2] U. Gradmann and J. Müller, Flat ferromagnetic, epitaxial 48Ni/52Fe (111) films of few atomic layer, *Phys. Status Solidi B* **27**, 313 (1968).
- [3] C. Chappert and P. Bruno, Magnetic anisotropy in metallic ultrathin films and related experiments on cobalt films, *J. Appl. Phys.* **64**, 5736 (1988).
- [4] N. Nakajima, N. Koide, T. Shidara, H. Miyauchi, H. Fukutani, A. Fujimori, K. Iio, T. Katayama, M. Nývlt, and Y. Suzuki, Perpendicular Magnetic Anisotropy Caused by Interfacial Hybridization Via Enhanced Orbital Moment in Co/Pt Multilayers: Magnetic Circular X-Ray Dichroism Study, *Phys. Rev. Lett.* **81**, 5229 (1998).
- [5] H. X. Yang, M. Chshiev, B. Dieny, J. H. Lee, A. Manchon, and K. H. Shin, First-principles investigation of the very large perpendicular magnetic anisotropy at Fe|MgO and Co|MgO interfaces, *Phys. Rev. B* **84**, 054401 (2011).
- [6] S. Z. Peng, M. X. Wang, H. X. Yang, L. Zeng, J. Nan, J. Q. Zhou, Y. G. Zhang, A. Hallal, M. Chshiev, K. L. Wang, Q. F. Zhang, and W. S. Zhao, Origin of interfacial perpendicular magnetic anisotropy in MgO/CoFe/metallic capping layer structures, *Sci. Rep.* **5**, 18173 (2015).
- [7] W. Lin, B. Yang, A. P. Chen, X. Wu, R. Guo, S. Chen, L. Liu, Q. Xie, X. Shu, Y. Hui, G. M. Chow, Y. Feng, G. Carlotti, S. Tacchi, H. Yang, and J. Chen, Perpendicular Magnetic Anisotropy and Dzyaloshinskii-Moriya Interaction at an Oxide/Ferromagnetic Metal Interface, *Phys. Rev. Lett.* **124**, 217202 (2020).
- [8] N. Nagaosa, J. Sinova, S. Onoda, A. H. MacDonald, and N. P. Ong, Anomalous Hall effect, *Rev. Mod. Phys.* **82**, 1539 (2010).
- [9] R. Karplus and J. M. Luttinger, Hall effect in ferromagnetics, *Phys. Rev.* **95**, 1154 (1954).
- [10] J. Smit, The spontaneous Hall effect in ferromagnetics I, *Physica (Amsterdam)* **21**, 877 (1955).
- [11] J. Smit, The spontaneous Hall effect in ferromagnetics II, *Physica (Amsterdam)* **24**, 39 (1958).
- [12] L. Berger, Side-jump mechanism for the Hall effect of ferromagnets, *Phys. Rev. B* **2**, 4559 (1970).
- [13] J. Moritz, B. Rodmacq, S. Auffret, and B. Dieny, Extraordinary Hall effect in thin magnetic films and its potential for sensors, memories and magnetic logic applications, *J. Phys. D: Appl. Phys.* **41**, 135001 (2008).
- [14] C. Zeng, Y. Yao, Q. Niu, and H. H. Weitering, Linear Magnetization Dependence of the Intrinsic Anomalous Hall Effect, *Phys. Rev. Lett.* **96**, 037204 (2006).
- [15] E. Roman, Y. Mokrousov, and I. Souza, Orientation Dependence of the Intrinsic Anomalous Hall Effect in hcp Cobalt, *Phys. Rev. Lett.* **103**, 097203 (2009).
- [16] H. Lu, A. Lipatov, S. Ryu, D. J. Kim, H. Lee, M. Y. Zhuravlev, C. B. Eom, E. Y. Tsymbal, A. Sinitskii, and A. Gruverman, Ferroelectric tunnel junctions with graphene electrodes, *Nat. Commun.* **5**, 5518 (2014).
- [17] Y. Tian, L. Ye, and X. F. Jin, Proper Scaling of the Anomalous Hall Effect, *Phys. Rev. Lett.* **103**, 087206 (2009).
- [18] S. Onoda, N. Sugimoto, and N. Nagaosa, Intrinsic versus Extrinsic Anomalous Hall Effect in Ferromagnets, *Phys. Rev. Lett.* **97**, 126602 (2006).
- [19] H. Li, B. W. Zhang, J. H. Liang, B. Ding, J. Chen, J. L. Shen, Z. F. Li, E. K. Liu, X. K. Xi, G. H. Wu, Y. Yao, H. X. Yang, and W. H. Wang, Large anomalous Hall effect in a hexagonal ferromagnetic Fe<sub>5</sub>Sn<sub>3</sub> single crystal, *Phys. Rev. B* **101**, 140409(R) (2020).
- [20] P. N. Dheer, Galvanomagnetic effects in iron whiskers, *Phys. Rev.* **156**, 637 (1967).
- [21] W. Jellinghaus, Einfluß der nachbarelemente des eisens auf den Hall-effekt eisenreicher mischkristalle, *Ann. Phys.* **462**, 189 (1961).
- [22] J. H. Yu, R. González-Hernández, L. Liu, J. Y. Deng, H. Y. Yoong, H. Wang, W. N. Lin, H. X. Liu, F. Poh, J. Sinova, and J. S. Chen, Thickness dependence of anomalous Hall conductivity in L1<sub>0</sub>-FePt thin film, *J. Phys. D: Appl. Phys.* **52**, 43LT02 (2019).
- [23] J. Y. Zhang, W. L. Peng, G. H. Yu, Z. B. He, F. Yang, W. Ji, C. Hu, and S. G. Wang, Tunable giant anomalous Hall angle in perpendicular multilayers by interfacial orbital hybridization, *ACS Appl. Mater. Interfaces* **11**, 24751 (2019).
- [24] S. Q. Zheng, K. K. Meng, Q. B. Liu, J. K. Chen, J. Miao, X. G. Xu, and Y. Jiang, Disorder dependent spin-orbit torques in L1<sub>0</sub> FePt single layer, *Appl. Phys. Lett.* **117**, 242403 (2020).
- [25] M.-C. Chang and Q. Niu, Berry phase, hyperorbits, and the Hofstadter spectrum: Semiclassical dynamics in magnetic Bloch bands, *Phys. Rev. B* **53**, 7010 (1996).
- [26] B. Zimmermann, N. H. Long, P. Mavropoulos, S. Blügel, and Y. Mokrousov, Influence of complex disorder on skew-scattering Hall effects in L1<sub>0</sub>-ordered FePt alloy, *Phys. Rev. B* **94**, 060406(R) (2016).
- [27] N. A. Sinitsyn, Semiclassical theories of the anomalous Hall effect, *J. Phys.: Condens. Matter* **20**, 023201 (2008).
- [28] D. Z. Hou, G. Su, Y. Tian, X. F. Jin, S. A. Yang, and Q. Niu, Multivariable Scaling for the Anomalous Hall Effect, *Phys. Rev. Lett.* **114**, 217203 (2015).

- [29] D. Yue and X. F. Jin, Towards a better understanding of the anomalous Hall effect, *J. Phys. Soc. Jpn.* **86**, 011006 (2017).
- [30] A. Crépieux and P. Bruno, Theory of the anomalous Hall effect from the Kubo formula and the Dirac equation, *Phys. Rev. B* **64**, 014416 (2001).
- [31] P. F. Carcia, Perpendicular magnetic anisotropy in Pd/Co and Pt/Co thin film layered structures, *J. Appl. Phys.* **63**, 5066 (1988).
- [32] B. Rodmacq, A. Manchon, C. Ducruet, S. Auffret, and B. Dieny, Influence of thermal annealing on the perpendicular magnetic anisotropy of Pt/Co/AIO<sub>x</sub> trilayers, *Phys. Rev. B* **79**, 024423 (2009).
- [33] P. M. Haney, H.-W. Lee, K.-J. Lee, A. Manchon, and M. D. Stiles, Current-induced torques and interfacial spin-orbit coupling, *Phys. Rev. B* **88**, 214417 (2013).
- [34] T. Lin, H. Liu, S. Poellath, Y. Zhang, B. Ji, N. Lei, J. J. Yun, L. Xi, D. Z. Yang, T. Xing, Z. L. Wang, L. Sun, Y. Z. Wu, L. F. Yin, W. B. Wang, J. Shen, J. Zweck, C. H. Back, Y. G. Zhang, and W. S. Zhao, Observation of room-temperature magnetic skyrmions in Pt/Co/W structures with a large spin-orbit coupling, *Phys. Rev. B* **98**, 174425 (2018).
- [35] Y. Du, H. Gamou, S. Takahashi, S. Karube, M. Kohda, and J. Nitta, Disentanglement of Spin-Orbit Torques in Pt/Co Bilayers with the Presence of Spin Hall Effect and Rashba-Edelstein Effect, *Phys. Rev. Appl.* **13**, 054014 (2020).
- [36] P. C. McIntyre, C. J. Maggiore, and M. Nastasi, Epitaxial of Pt thin films on (001) MgO—I. Interface energetics and misfit accommodation, *Acta Mater.* **45**, 869 (1997).
- [37] B. M. Lairson, M. R. Visokay, R. Sinclair, S. Hagstrom, and B. M. Clemens, Epitaxial Pt(001), Pt(110), and Pt(111) films on MgO(001), MgO(110), MgO(111), and Al<sub>2</sub>O<sub>3</sub>(0001), *Appl. Phys. Lett.* **61**, 1390 (1992).
- [38] See Supplemental Material at <http://link.aps.org/supplemental/10.1103/PhysRevB.104.214417> for details on the efficient structural regulating effect of the Cr insertion, structural properties of the Pt top layer, and magnetic proximity effect in Pt/Co/Pt trilayers. This includes Ref. [39].
- [39] Y. C. Zhao, H. C. Lyu, G. Yang, B. W. Dong, J. Qi, J. Y. Zhang, Z. Z. Zhu, Y. Sun, G. H. Yu, Y. Jiang, H. X. Wei, J. Wang, J. Lu, Z. H. Wang, J. W. Cai, B. G. Shen, W. S. Zhan, F. Yang, S. J. Zhang, and S. G. Wang, Direct observation of magnetic contrast obtained by photoemission electron microscopy with deep ultra-violet laser excitation, *Ultramicroscopy* **202**, 156 (2019).
- [40] J. Kötzler and W. Gil, Anomalous Hall resistivity of cobalt films: Evidence for the intrinsic spin-orbit effect, *Phys. Rev. B* **72**, 060412(R) (2005).
- [41] L. Ye, Y. Tian, X. F. Jin, and D. Xiao, Temperature dependence of the intrinsic anomalous Hall effect in nickel, *Phys. Rev. B* **85**, 220403(R) (2012).
- [42] T. H. Dang, J. Hawecker, E. Rongione, G. Baez Flores, D. Q. To, J. C. Rojas-Sanchez, H. Nong, J. Mangeney, J. Tignon, F. Godel, S. Collin, P. Seneor, M. Bibes, A. Fert, M. Anane, J. M. George, L. Vila, M. Cosset-Cheneau, D. Dolfi, R. Lebrun *et al.*, Ultrafast spin-currents and charge conversion at 3d-5d interfaces probed by time-domain terahertz spectroscopy, *Appl. Phys. Rev.* **7**, 041409 (2020).
- [43] T. H. Dang, Q. Barbedienne, D. Q. To, E. Rongione, N. Reyren, F. Godel, S. Collin, J. M. George, and H. Jaffrès, Anomalous Hall effect in 3d/5d multilayers mediated by interface scattering and nonlocal spin conductivity, *Phys. Rev. B* **102**, 144405 (2020).
- [44] E. Sagasta, Y. Omori, M. Isasa, M. Gradhand, L. E. Hueso, Y. Niimi, Y. Otani, and F. Casanova, Tuning the spin Hall effect of Pt from the moderately dirty to the superclean regime, *Phys. Rev. B* **94**, 060412(R) (2016).
- [45] L. J. Zhu, D. C. Ralph, and R. A. Buhrman, Irrelevance of magnetic proximity effect to spin-orbit torques in heavy-metal/ferromagnet bilayers, *Phys. Rev. B* **98**, 134406 (2018).
- [46] M. Chen, Z. Shi, J. W. Xu, X. X. Zhang, J. Du, and S. M. Zhou, Tuning anomalous Hall conductivity in L1<sub>0</sub> FePt films by long range chemical ordering, *Appl. Phys. Lett.* **98**, 082503 (2011).
- [47] P. Li, L. J. Riddiford, C. Bi, J. J. Wissler, X.-Q. Sun, A. Vailionis, M. J. Veit, A. Altman, X. Li, M. DC, S. X. Wang, Y. Suzuki, and S. Emori, Charge-spin interconversion in epitaxial Pt probed by spin-orbit torques in a magnetic insulator, *Phys. Rev. Mater.* **5**, 064404 (2021).
- [48] Q. Zhang, D. X. Zheng, Y. Wen, Y. L. Zhao, W. B. Mi, A. Manchon, O. Boulle, and X. X. Zhang, Effect of surface roughness on the anomalous Hall effect in Fe thin films, *Phys. Rev. B* **101**, 134412 (2020).
- [49] S. Forster, K. Meinel, R. Hammer, M. Trautmann, and W. Widdra, Quasicrystalline structure formation in a classical crystalline thin-film system, *Nature (London)* **502**, 215 (2013).
- [50] Y. S. Xie, B. W. Zhu, J. Liu, Z. L. Xu, and X. W. Wang, Thermal reffusivity: Uncovering phonon behavior, structural defects, and domain size, *Front. Energy* **12**, 143 (2018).
- [51] M. Belhadi, A. Khater, O. Rafil, and J. Hardy, Scattering of phonons in hexagonal 2D crystals on their domain boundaries, *Phys. Status Solidi B* **228**, 685 (2001).
- [52] A. Casaca, G. Bonfait, C. Dubourdieu, F. Weiss, and J. P. Sénateur, Magnetoresistance and Hall effect in unidirectionally twinned YBa<sub>2</sub>Cu<sub>3</sub>O<sub>7</sub> thin films, *Phys. Rev. B* **59**, 1538 (1999).